FFT-based simulations of heterogeneous conducting materials with combined non-uniform Neumann, Periodic and Dirichlet boundary conditions

Lionel Gelebart

FFT-based simulations of heterogeneous conducting materials with combined non-uniform Neumann, Periodic and Dirichlet boundary conditions

Lionel Gélébart

Université Paris-Saclay, CEA, SRMA, 91191, GIF/YVETTE, FRANCE

Email : lionel.gelebart@cea.fr

Abstract:

Because of their simplicity, efficiency and ability for parallelism, FFT-based methods are very attractive in the context of numerical periodic homogenization, especially when compared to standard FE codes used in the same context. The purpose of the paper is to go beyond the use of periodic Boundary Conditions (BC), but keeping the advantages of FFT-based implementations. The present paper focuses on conductivity problems, considered as a first step towards mechanical problems. The proposed implementation is highly flexible, allowing to apply non-uniform loadings, to choose between periodic, Neumann and Dirichlet BC for each face of the unit-cell (of couple of faces for periodic BC), and to choose between different types of Finite Differences schemes (two types are considered here). The implementation relies on the use of Discrete Trigonometric Transforms (i.e. sine and cosine transforms) and their relation with the Discrete Fourier Transform on 4 times extended signals. The use of DTTs implicitly considers the signal to be anti-symmetric or symmetric with respect to each domain boundary. A direct relationship exists between the choice of a DTT (among 16 available) used in a given direction and the type of symmetry assumed on each boundary. Symmetry and anti-symmetry assumptions are respectively related to Dirichlet BC and anti-symmetry. The implementation has been precisely validated for various types of loading (uniform or non-uniform, full or combined, Dirichlet, Neumann and periodic BC) from a direct comparison with the same FE simulations.

Keywords: heterogeneous material, FFT, Periodic, Neumann, Dirichlet, thermal conductivity

1 – Introduction

Solving mechanical problems defined on heterogeneous unit-cells, submitted to periodic BC, with FFT-based algorithm was proposed initially by Moulinec and Suquet [12]. Its application to conducting materials is straightforward, and even simpler as the size of the tensors is decreased compared to mechanics (i.e vectors replaced by scalar, second order tensors by vectors etc…). Because of their simplicity, efficiency and ability for parallelism, they have become very popular and various improvements have been proposed since the original proposition. The reader is invited to read the review papers of Schneider [15], Lucarini [10] or Gierden [7], for an overview of the different advances.

An important limitation of current FFT-based implementations is their restriction to periodic BC. To circumvent that problem, the unit-cell can be embedded in a buffer whose properties can be adjusted to simulate Neumann BC (see for example [4] for a simulation on a tube), or combined to a modified algorithm, to simulate Dirichlet BC [6]. Using a buffer zone is also proposed by To [17] [16] with a rather different method, using form factors. Very recently, the question was addressed differently for conducting materials by Monchiet [11]: instead of using a buffer, the unit-cell and the loading is duplicated and symmetrized consistently with the type of BC (Neumann or Dirichlet). The advantage is that a classical FFT-based implementation can be used 'as it is', the drawback is that the unit-cell is multiplied by 8 in 3D. In addition, their proposition is limited to uniform BC. Another approach was proposed recently by Grimm-Strele [9], for mechanical problems, in order to apply orthogonal mixed uniform BC proposed by Pahr [13]. This approach extends the previous works of Wiegmann [2] to heterogeneous materials: in that case, fields are implicitly symmetrized with the use of discrete Sine and Cosine transforms, similarly to the use of the discrete Fourier Transform. However, the implementation was limited to uniform loadings and to a limited number of loading cases. Note that a similar approach was also recently followed by Wise [20] for solving the wave propagation equation in a homogeneous medium with various types of BC and a Pseudo Spectral Time Derivative solver. Following the same approach for heterogeneous conducting materials, the aim of the paper is to propose a highly flexible implementation, allowing to apply non-uniform loadings, to choose between periodic, Neumann and Dirichlet BC for each face of the unit-cell (of couple of faces for periodic BC), and to choose between different types of Finite Differences schemes (two types are considered here).

The position of any point M is given by a vector $\boldsymbol{x}$, whose coordinates (x_1, x_2, x_3) are related to an orthonormal coordinate system $(O, \boldsymbol{e_1}, \boldsymbol{e_2}, \boldsymbol{e_3})$. The unit cell consists of a parallelepiped of dimensions L_1, L_2 and L_3. The unit-cell is bounded by 6 faces denoted S_d^0 and S_d^1 $(d = 1{:}3)$: S_d^0 with an outer normal vector $\boldsymbol{N_d^0} = -\boldsymbol{e_d}$, positioned at $(x_d = 0)$, and S_d^1 positioned at $x_d = L_d$ with a normal $\boldsymbol{N_d^1} = -\boldsymbol{e_d}$. The field equations governing the conduction problem are reported below:

$$\begin{cases} \operatorname{div}(\boldsymbol{q}) = 0 \\ \boldsymbol{q} = -\underline{K}.\boldsymbol{\nabla T} \\ T = T^* + \tilde{T} \end{cases} \tag{1}$$

with $\boldsymbol{q}$ the heat flux, T the temperature and $\underline{K}$ the heterogeneous thermal conductivity. Note that an arbitrary given field T^* is introduced, so that the unknown field is the temperature fluctuation $\tilde{T}$.

Different boundary conditions (BC) can be associated to each face (or couple of faces). For periodic BC on faces S_d^0 and S_d^1, $\tilde{T}$ and $\boldsymbol{q}.\boldsymbol{e_d}$ have to be L_d-periodic (same value on opposite points). For Dirichlet

BC on a given surface S_d^j, the fluctuation $\tilde{T}$ is null on S_d^j (so that the value of T corresponds to T^*). For Neumann BC on a given surface S_d^j, the normal heat flux $\boldsymbol{q}.\boldsymbol{N_d^j}$ must be equal to an arbitrary applied flux Q_d^*. The standard implementation of FFT-based methods for the simulation of heterogeneous materials only considers periodic BC on the 3 couples of faces. The proposed implementation allows for every combinations of BC on the 6 different faces. With 5 combinations per couple of opposite faces (Periodic, Dirichlet/Dirichlet, Dirichlet/Neumann, Neumann/Dirichlet and Neumann/Neumann) the implementation has to be flexible enough to account for 125 possible combinations (250 in fact as two discretization schemes will be considered). This flexibility comes from the fact that all these boundary conditions can be regarded as periodic boundary conditions on 2 or 4 times larger unit-cells using appropriate symmetries. At the centre of the proposed implementation, the FFT-based algorithm used with periodic BC is briefly summarized below.

Solving problem (1) with periodic boundary conditions, using a regular spatial discretization of the fields over the unit-cell, can be done with Discrete Fourier Transform (with the notation $DFT(f) = \hat{f}^{DFT}$ or simply $\hat{f}$) as follows:

$$\begin{cases} \boldsymbol{q} = -\underline{K}.(\boldsymbol{\nabla_D} \boldsymbol{T}^* + \boldsymbol{\nabla_D}\tilde{\boldsymbol{T}}) \\ p = \mathrm{div_D}\left(\boldsymbol{q} - k_0 \boldsymbol{\nabla_D}\tilde{\boldsymbol{T}}\right) \\ \mathrm{div_D}\left(\boldsymbol{\nabla_D}\tilde{\boldsymbol{T}}\right) = -\dfrac{p}{k_0} \end{cases} \Leftrightarrow \begin{cases} \boldsymbol{q} = -\underline{K}.\left(\boldsymbol{\nabla_D} \boldsymbol{T}^* + \boldsymbol{\nabla_D}\tilde{\boldsymbol{T}}\right) \\ p = \mathrm{div_D}\left(\boldsymbol{q} - k_0 \boldsymbol{\nabla_D}\tilde{\boldsymbol{T}}\right) \\ \hat{\tilde{\mathrm{T}}} = \dfrac{\hat{p}}{k_0 \|\boldsymbol{\xi_D}\|^2} (\doteq \hat{G}_D(\hat{p})) \end{cases} \quad (2)$$

In the present formulation (2), all the variables are discrete fields, $\mathrm{div_D}$ and $\boldsymbol{\nabla_D}$ stand for discrete divergence and gradient operators associated to the choice of a finite discretization D. With this choice comes the definition of modified wave-vectors $\boldsymbol{\xi_D}$, so that $\widehat{\mathrm{div_D}(\boldsymbol{q})} = \mathrm{i}\hat{\boldsymbol{q}}.\boldsymbol{\xi_D}$ and $\widehat{\boldsymbol{\nabla_D} \boldsymbol{T}} = \mathrm{i}\hat{T}\boldsymbol{\xi_D}$. Their expressions can be found in [19] or [15] for different finite discretization schemes. Formulation (2) allows for the definition of a fix-point algorithm: first step, given $\tilde{T}$ evaluate p in real space, second step, apply the discrete Green operator (i.e. evaluate $\tilde{T}$ from a back and forth in Fourier space), back to first step. The choice of the numerical parameter k_0 affects the convergence of the fix-point algorithm [12], however, using an acceleration convergence procedure (the Anderson's acceleration as proposed in [4] and implemented in [8]) drastically accelerates the convergence and reduces its sensitivity to k_0.

After introducing the geometric discretization and the two Finite Differences (FD) schemes used in the present paper, the second step of the algorithm (apply Green operator $\hat{\tilde{\mathrm{T}}} = \hat{G}_D(\hat{p})$) is first detailed, using Discrete Trigonometric Transforms to account for different types of symmetries in the evaluation of the discrete Green operator, G_D. Then, the first step (evaluate p in equation (2)) is described, using symmetries to extend the size of the unit-cell and evaluate discrete derivatives in real space. Finally, after a section devoted to additional remarks, comes the final validation with various different loadings demonstrating the flexibility of the implementation.

2 – Unit-cell discretization and Finite Differences schemes

Figure 1, illustrates the definitions used for the discretization of the unit-cell. The grid of nodes touches the boundaries of the unit-cell, whereas the grid of centres, translated by half a voxel do not touch the boundary. The size of the grid of centres is $n_1 n_2 n_3$ with the range $[0: n_d - 1]_{d=1:3}$, and the size of the

grid of nodes is $(n_1+1)(n_2+1)(n_3+1)$ with the range $[0{:}\,n_d]_{d=1:3}$ (with notation $[0{:}\,n_d]_{d=1:3} = [0{:}\,n_1]\times[0{:}\,n_2]\times[0{:}\,n_3]$ and $0{:}\,n = \{0,1,2,\dots,n\}$).

Two Finite Differences (FD) schemes are used: the "Octahedral" scheme corresponds to the classical first order centered derivation scheme (points involved in the derivation are placed on an octahedron), with the notation O replacing D in (2), and the "Hexahedral" scheme, strictly equivalent to the first order derivation obtained using hexahedral finite elements with reduced integration [14], with notation H (points involved in the derivation are placed on an hexahedron). These different schemes are represented in Figure 1, on which important remarks are made:

- For the O-scheme, all the quantities $(\tilde{T}, \boldsymbol{\nabla_D T}, \boldsymbol{q}, p)$ are defined on the grid of nodes, whereas for the H-scheme, the quantities $(\tilde{T}, p)$ and $(\boldsymbol{\nabla_D T}, \boldsymbol{q})$ are defined on the grid of nodes and the grid of centres, respectively.
- The evaluation of the heat flux $\boldsymbol{q} = -\underline{K}.\boldsymbol{\nabla_D T}$ supposes $\underline{K}$ and $\boldsymbol{\nabla_D T}$ defined on the same grid. So, as a consequence of the previous point: for the H-scheme, $\underline{K}$ is evaluated on the grid of centres and for the O-scheme, $\underline{K}$ is evaluated on the grid of nodes. Hence, the discretization of the material properties is slightly different depending on the FD scheme.
- For the O-scheme, evaluation of derivatives at the boundary requires the knowledge of quantities outside of the domain. For the H-scheme, only the derivation of $\boldsymbol{\nabla_D T}$ or $\boldsymbol{q}$, defined at centers, requires quantities defined outside of the domain. In both cases, these quantities are defined according to the symmetry conditions associated to the choice of BC (see next sections).

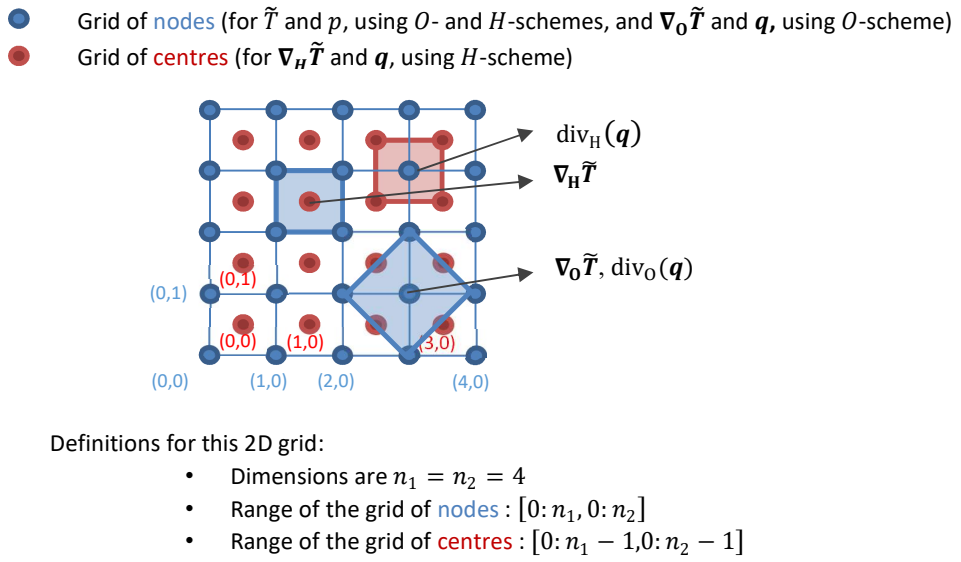

Definitions for this 2D grid:

- Dimensions are $n_1 = n_2 = 4$
- Range of the grid of nodes : $[0{:}\,n_1, 0{:}\,n_2]$
- Range of the grid of centres : $[0{:}\,n_1 - 1, 0{:}\,n_2 - 1]$

Figure 1 : Illustration of the unit-cell discretization: definition of the ranges of the grids of corners and centres, locations of the different quantities depending on the Finite Difference scheme (O or H), and illustration of the O and H schemes.

Using periodic boundary conditions in the 3 directions, with $\tilde{T}$ defined on the range $[0{:}\,n_d - 1]_{d=1:3}$, the modified wave-vectors for the two schemes, $\boldsymbol{\xi_O}$ and $\boldsymbol{\xi_H}$, can be found in [19] or [15].

Defining problem (1) on a M times larger unit-cell and keeping the same grid discretization (i.e. with the range $[0{:}\,Mn_i - 1]_{i=1:3}$), the modified wave-vectors will be noted as $\boldsymbol{\xi_{DM}}$ (in practice M will be 2 or 4).

3 – Application of the Green Operator with symmetry conditions

Solving $\mathrm{div_D}\left(\boldsymbol{\nabla_D}\widetilde{\boldsymbol{T}}\right) = -\frac{p}{k_0}$ is equivalent to write $\tilde{T} = G_D(p)$, with G_D a discrete Green operator (non-local). Evaluating the Green operator can be done straightforwardly with DFT if periodic BC are prescribed (see equation (2)). The aim of the present section is to build the discrete Green operator with non-periodic BC. It makes use of Discrete Trigonometric Transform (DTT), which can be related to standard DFT on larger unit-cells.

Note that below, DTTs gathers sine and cosine discrete transforms, and DTs, for discrete transforms, gathers the DTTs and the DFT.

Notations for discrete symmetry types and their associated DTTs

For a 1D discrete signal, the definitions of symmetry extensions outside of the domain depends: on the type of symmetry, which can be A (for Anti-symmetry) or S (for Symmetry), but also on the position of the (anti-)symmetry axis, whether located on an ending point, notation W (for Whole), or a half-element after, notation H (for Half). Assuming that the location of the symmetry axis has the same location type T (whether W or H), the notation TXTY specifies the symmetry type with X and Y (whether A or S) respectively for the left (first) and right (or last) point of the discrete signal. In that case, the number of different combinations is of 8. As an example, the notation WAWS assumes an extension of the discrete signal with anti-symmetry (A) on the left side and symmetry (S) on the right side, the symmetry axis being located on the ending points (W). In addition, it must be noted that each type of symmetry extension corresponds to the definition of a given DTT (see [5] and [20]) and can also be associated to a type of boundary condition (Dirichlet or Neumann) as seen in equation (10). *Table* 1 gathers all these informations. Finally, in case of 2D (or 3D) discrete fields, the symmetry is related to a given direction d ($d = 1{:}\,3$, in 3D) with the notation $\mathrm{TX_dTY_d}$.

In addition, various graphical representations are given in appendix to visualize these symmetries and accommodate with the notation.

Discrete symmetry type (TXTY)	Discrete Trigo. Transf. [5]	Boundary Condition (left/right)
WSWS	DCT1	Dirichlet/Dirichlet
HSHS	DCT2	
WSWA	DCT3	Dirichlet/Neumann
HSHA	DCT4	
WAWA	DST1	Neumann/Neumann
HAHA	DST2	
WAWS	DST3	Dirichlet/Neumann
HAHS	DST4	

Table 1 : The table gathers the different discrete symmetry types (T=W or H for the location of symmetry axis, X=S or A for the type of symmetry on the left side, and Y=S or A for the right side), see explanations in the next for a more detailed description of the notation), the corresponding type of DT according to the names defined in the fftw library [5], and the associated types of boundary conditions, see equation (10).

3.1 – DFT

The definition of the 1D DFT $\hat{F}$, of a sequence of n points f, associated to the definition of the wave-number ξ_j, is:

$$\hat{F}_k = \sum_{j=0}^{n-1} f_j \exp(-\mathrm{i}k\xi_j), \qquad \xi_j = \frac{2\pi j}{n}, \qquad k \in [0: n-1] \tag{3}$$

Extending this definition to 3D consists of applying 1D FFTs, separately in each direction, so that the definition, together with the definition of wave-vectors $\boldsymbol{\xi_j}$, becomes:

$$\hat{F}_{\boldsymbol{k}} = \sum_{\boldsymbol{j} \in [0: n_d - 1]_{d=1:3}} f_{\boldsymbol{j}} \exp(-\mathrm{i}\boldsymbol{k}.\boldsymbol{\xi}_j), \qquad \boldsymbol{\xi_j} = \left(\frac{2\pi j_1}{n_1}, \frac{2\pi j_2}{n_2}, \frac{2\pi j_3}{n_3}\right), \qquad \boldsymbol{k} \in [0: n_d - 1]_{d=1:3} \tag{4}$$

As proposed in the previous section, we use the notation $\hat{F}_M$ for the DFT of a signal with range $[0: Mn - 1]$. Note that the definition of the wave number $\xi_{M,j}$ is deduced from the definition of ξ_j as follows:

$$\hat{F}_{M,k} = \sum_{j=0}^{Mn-1} f_j \exp(-\mathrm{i}k\xi_{M,j}), \qquad \xi_{M,j} = \frac{2\pi j}{Mn}, \qquad k \in [0: Mn - 1] \tag{5}$$

3.2 – DCT1 (WSWS)

The definition of the Discrete Cosine Transform of type 1, or DCT1, is associated to the extension of the signal defined on the range $[0: n]$ to the range $[0: 2n - 1]$ that is assumed periodic (see appendix). Filling the extension is done according to symmetry assumptions on both sides of the initial domain. For DCT1, the left point $(i = 0)$, belongs to the symmetry axis (W) and Symmetry (S) is assumed, this explain the first part of WSWS. The right point $(i = n)$ has the same properties which explain the second part of WSWS. Note that W stands for "whole" when the symmetry axis crosses the "whole" point. H stands for "half" when the axis crosses between two points. With the symmetry WSWS, the extension is filled according to the relation: $f_{n+j} = f_{n-j}$ for $j \in [0: n]$.

Applying the DFT definition (5) on the twice ($M = 2$) extended signal (with range $[0: 2n - 1]$ for j and k) and using the relation $f_{n+j} = f_{n-j}$ leads (after simple manipulations) to the definition of the DCT1 (as used in the library *fftw* [5]):

$$\hat{F}_{2,k} = f_0 + f_{N-1}(-1)^k + 2\sum_{j=1}^{N-2} f_j \cos\left(\frac{k\pi j}{N-1}\right) = \hat{F}_k^{DCT1}, \qquad k \in [0: n], \tag{6}$$

with N the number of points in the initial sequence (*i.e.* $N = n + 1$). DCT1 is performed on f_j, for the complete range $j \in [0: n]$.

3.3 – DST1 (WAWA)

On the difference to the previous case, the twice extended signal is filled with anti-symmetry assumptions on left and right points (see appendix), leading to the relation: $f_{n+j} = -f_{n-j}$ for $j \in [0:n]$. This condition necessitates that the signal vanishes on extreme points: $f_0 = f_n = 0$. Following the same procedure as for DCT1 leads to the definition of DST1 (as used in *fftw* [5]):

$$\hat{F}_{2,k} = -\mathrm{i}.\,2\sum_{j=0}^{N-1} f_j^* \sin\left(\frac{k\pi(j+1)}{N+1}\right) = -\mathrm{i}\hat{F}_{k-1}^{DST1}, \qquad k \in [1:n-1], \tag{7}$$

with N the number of non-vanishing points in the initial sequence (*i.e.* $N = n-1$). Actually, in that case, DST1 is performed on f_j, for a reduced range $j \in [1:n-1]$, excluding f_0 and f_n necessarily set to 0. Equation (7) uses a renumbering with $f_j^* = f_{j+1}$ for $j \in [0:N-1] (= [0:n-2])$.

3.4 – DCT3 (WSWA)

In the previous cases, the symmetry conditions were the same on both sides. Now, the conditions are symmetry on left point and anti-symmetry on right point. Hence, the signal must be extended 4 times, from the range $[0:n]$ to the range $[0:4n-1]$, to obtain a periodic signal consistent with the symmetry conditions (see appendix). For each quarter of the extended signal we use the relations deduced from the symmetry conditions: $f_{n+j} = -f_{n-j}$, $f_{2n+j} = -f_j$ and $f_{3n+j} = f_{n-j}$, for $j \in [0:n]$. Note that the first condition necessitates $f_n = 0$. Following the same procedure as before, but with a 4 times extension (*i.e.* $M = 4$), leads to the definition of DCT3 (as used in *fftw* [5]):

$$\hat{F}_{4,2k+1} = 2\left(f_0 + \sum_{j=1}^{n-1} f_j \cos\left(\frac{\pi(k+1/2)j}{n}\right)\right) = 2\hat{F}_k^{DCT3}, \qquad k \in [0:n-1]. \tag{8}$$

Here, DCT3 is performed on f_j for a reduced range $j \in [0:n-1]$, excluding f_n necessarily set to 0.

3.5 – DST3 (WAWS)

DST3 is defined using the same procedure as DCT3, with the symmetry relations, $f_{n+j} = f_{n-j}$, $f_{2n+j} = -f_j$ and $f_{3n+j} = -f_{n-j}$, for $j \in [0:n]$. The last relation, together with the periodicity condition over the extended domain ($f_0 = f_{4n}$), necessitates $f_0 = 0$. Similar to DST3, the definition of DCT3 reads:

$$\hat{F}_{4,2k+1} = -2\mathrm{i}\left(f_{n-1}^*(-1)^k + 2\sum_{j=0}^{n-2} f_j^* \sin\left(\frac{\pi(j+1)\left(k+\frac{1}{2}\right)}{n}\right)\right) = -2\mathrm{i}\hat{F}_k^{DST3}, k \in [0:n-1]. \tag{9}$$

DST3 is performed on f_j for a reduced range $j \in [1:n]$, excluding f_0 necessarily set to 0. Equation (9) uses a renumbering with $f_j^* = f_{j+1}$for $j \in [0:n-1]$.

3.6 – Relations between the symmetries of f and its derivatives

For the sake of clarity, 2D fields are considered (adaptation to 3D or 1D fields being straightforward). Notation $\mathrm{TX_dTY_d}$ used below is detailed at the beginning of section 3. If a field f has the symmetries $\mathrm{TX_1TY_1/TX_2TY_2}$, for direction 1/direction 2, with $\mathrm{X_i}$ and $\mathrm{Y_i}$ the type of symmetry (A or S) and T the location of the symmetry (W or H, for field defined at nodes or at centers), then, the symmetry is inverted in the direction of derivation and kept in the other direction. In other words, df/dx_1 has the symmetry $\mathrm{T\overline{X}_1T\overline{Y}_1/TX_2TY_2}$ and df/dx_2 the symmetry $\mathrm{TX_1TY_1/T\overline{X}_2T\overline{Y}_2}$, with the notation $\overline{\mathrm{A}} = \mathrm{S}$ and $\overline{\mathrm{S}} = \mathrm{A}$.

For example, assuming a field f with the symmetry $\mathrm{WSWA/WAWA}$ (i.e. a field defined at nodes (W), Symmetric (S) and Anti-symmetric (A) on the left and right sides in direction 1, and Anti-symmetric on both sides in direction 2), the derivative df/dx_1 has the symmetry WAWS/WAWA and df/dx_2 has the symmetry WSWA/WSWS.

Note that above, the location T is not modified by the derivative, which corresponds to a Finite Difference scheme for which the quantity and its derivative is evaluated at the same physical point (the nodes here), such as the O-scheme used in the present paper. Alternatively, the derivative can be evaluated at centers, between the nodes where the quantities are given (see Figure 1), or conversely at nodes if quantities are given at centers. This is the case of the H-scheme, for which the derivation 'inverts' location T in $\overline{\mathrm{T}}$ (with the notation $\overline{\mathrm{W}} = \mathrm{H}$ and $\overline{\mathrm{H}} = \mathrm{W}$).

A general rule, useful for a flexible implementation, is proposed below. If a 3D field, f, has the symmetries $\mathrm{TX_1TY_1/TX_2TY_2/TX_3TY_3}$, its derivative in direction $\mathrm{d_0}$, df/dx_{d_0}, exhibits :

- inverse symmetry types in direction d_0 ($\overline{\mathrm{X}}_{\mathrm{d_0}}$ and $\overline{\mathrm{Y}}_{\mathrm{d_0}}$) and no inversion in the other directions,
- for H-scheme, an inverse symmetry location $\overline{T}$ (no inversion for the O-scheme).

3.7 – Relations between symmetries and non-periodic BC

As mentioned in the previous sub-sections, the WA symmetry condition is associated to a null value at the boundary: $\tilde{T}_0 = \tilde{T}_n = 0$ for WAWA, $\tilde{T}_0 = 0$ for WAWS, and $\tilde{T}_n = 0$ for WSWA. Hence, using the DTT associated to the anti-symmetry conditions, supposes implicitly a null Dirichlet BC that is $\tilde{T} = 0$.

According to the previous subsection, if a 1D field $\tilde{T}$ has a WS symmetry condition then $g = d\tilde{T}/dx$ has a WA or HA symmetry (whether the O- or H-scheme is used). As noticed just before, the WA symmetry is associated to a null value at the boundary. For the HA symmetry, the relation is (for the left point) $g_{-1} = -g_0$. However, located at centers g_{-1} and g_0 are defined on both side of the boundary so that the value at the middle point, that falls on the boundary, is evaluated by $g_{-1/2} = (g_0 + g_{-1})/2 = 0$. For 3D fields, applying a WS symmetry in direction d is equivalent to a null Neumann condition that is $\boldsymbol{\nabla_D \tilde{T}}.\boldsymbol{N_d} = 0$ (with $\boldsymbol{N_d}$ the outer normal to the boundary in direction d).

In brief, applying null Neumann or Dirichlet BC on $\tilde{T}$ can be done assuming appropriate symmetries for $\tilde{T}$ as follows:

$$\begin{aligned} &\mathrm{S\ symmetry\ for}\ \tilde{T} \implies \mathrm{null\ Neumann\ BC}\ (\boldsymbol{\nabla_D \tilde{T}}.\boldsymbol{N_d} = \boldsymbol{0}) \\ &\mathrm{A\ symmetry\ for}\ \tilde{T} \implies \mathrm{null\ Dirichlet\ BC}\ (\tilde{\boldsymbol{T}} = \boldsymbol{0}) \end{aligned} \tag{10}$$

3.8 – Green operator with null-Dirichlet, null-Neumann and Periodic BC

This section describes step by step the application of the Green operator $\tilde{T} = G_D(p)$, assuming that p and $\tilde{T}$ are 1D fields with the same range $[0:n]$, and the same symmetries (i.e. BC).

The connections established in the previous sub-sections between various DTs and DFT can be summarized as follows:

$$S_{4F}(\hat{p}_4^{DFT}) = \alpha\widehat{S_R(p)}^{DT} \tag{11}$$

S_R is a selection operator for arrays in real space. The range of p is $[0:n]$ and the range of $S_R(p)$ is $[0:N-1]$, with N the number of selected points. The points selected by S_R for each DT (see previous sub-sections) are gathered in Table 2.

S_{4F} is a selection operator for arrays in Fourier space and 4 times extended unit-cells. The range of $\hat{p}_4^{DFT}$ is $[0:4n-1]$ and $S_{4F}(\hat{p}_4^{DFT})$ is an array of range $[0:N-1]$, with N the number of selected points. The points selected by S_{4F} for each DT are gathered in Table 2. Note that in the previous subsections, selection is made for different extension factor : 1 (trivially, for DFT), 2 (for DCT1 and DST1) or 4 (for DCT3 and DST3). To simplify, selection is performed for the same extension factor $M = 4$ (i.e. in the same range $[0:4n-1]$), assuming 4 periodic repetitions for DFT, and 2 for DCT1 and DST1). Then the selection is done by multiplying by 2 (for DCT1 and DST1) or 4 (for DFT) the ranges selected for $M = 2$ or $M = 1$, as done in Table 2.

The factor α is not reported in Table 2 as its effect will be annihilated by a factor $1/\alpha$ in a further step (equation (13)). It can be easily deduced from previous sub-sections.

Once a selected range of Fourier coefficients $S_{4F}(\hat{p}_4^{DFT})$ has been evaluated from DT applications (equation (11)), the Green operator $\hat{G}_{D4}$ is applied for the same selection range:

$$S_{4F}\left(\hat{\tilde{T}}_4^{DFT}\right) = S_{4F}\left(\hat{G}_{D4}\hat{p}_4^{DFT}\right) = S_{4F}\left(\hat{G}_{D4}\right)S_{4F}(\hat{p}_4^{DFT}) = \frac{S_{4F}(\hat{p}_4^{DFT})}{k_0\|S_{4F}(\xi_{D4})\|^2} \tag{12}$$

where ξ_{D4} are the modified wave-numbers evaluated for a 4 times extended domain.

Equation (11) is now applied to deduce $\widehat{S_R(\tilde{T})}^{DT}$ from $S_{4F}\left(\hat{\tilde{T}}_4^{DFT}\right)$ according to:

$$\widehat{S_R(\tilde{T})}^{DT} = \frac{S_{4F}\left(\hat{\tilde{T}}_4^{DFT}\right)}{\alpha} \tag{13}$$

Then, inverse DT can be applied to $\widehat{S_R(\tilde{T})}^{DT}$ to obtain $S_R(\tilde{T})$.

Finally, the points which have not been selected by S_R in $[0:n]$, that corresponds to points located at the boundaries, must be filled: in case of Dirichlet BC on 0 and/or n, then $\tilde{T}_0 = 0$ and/or $\tilde{T}_n = 0$, in case of periodic BC, then $\tilde{T}_n = \tilde{T}_0$.

For the sake of simplicity, the presentation was done in 1D. However, the extension to 3D is rather straightforward and relies on the fact that the 3D transform corresponds to a succession of 1D transforms in each direction (with appropriate DT corresponding to the BC in each direction). The selection operators S_R and S_{4F} now operates on 3D arrays with the selection rules proposed in Table 2 for each direction. In equation (12), the wave-number ξ_{D4} in 1D is replaced by the wave-vector $\boldsymbol{\xi_{D4}}$, whose definition is given in [19] [15].

In terms of implementation, it must be emphasized that if 4 times extended fields are considered in Fourier space, only the values selected by S_{4F} appear in equations (11)(12)(13), and each quantity of type $S_{4F}(\hat{X}_4)$ corresponds to a 3D array of range $[0: N_d - 1]_{d=1:3}$, with N_d the number of points used in DT (see Table 2). Note that the array $S_{4F}(\boldsymbol{\xi_{D4}})$ in equation (12) corresponds to a selection of wave-vectors that can be evaluated once, at the beginning of the iterative fix-point algorithm.

To summarize, assuming that p and $\tilde{T}$ have the same symmetries, the application of the (non local) Green operator $\tilde{T} = G_D(p)$ is rather simple and flexible as soon as the selection operators S_R and S_{4F} are correctly initialized in agreement with Table 2. The four steps are:

- DT on a selected range (S_R) of p (→ equation (11)),
- Application of the Green Operator, for selected (S_{4F}) wave-vectors (→ equation (12)),
- Inverse DT (of equation (13)), to obtain $\tilde{T}$ on the selected range (S_R),
- Adjust non-selected points (for Dirichlet and Periodic BC).

DT	S_R : selection in $[0: n]$ (Real space)	S_F : selection in $[0,4n-1]$ (Fourier space)		N : number of selected points
WSWS / DCT1	$[0: n]$	$2 \times [0: n]$	$(0,2,4 \dots, 2n)$	$n+1$
WSWA / DCT3	$[0: n-1]$	$2 \times [0: n-1]+1$	$(1,3,5 \dots, 2n-1)$	n
WAWA / DST1	$[1: n-1]$	$2 \times [1: n-1]$	$(2,4,6 \dots, 2n-2)$	$n-1$
WAWS / DST3	$[1: n]$	$2 \times [0: n-1]+1$	$(1,3,5 \dots, 2n-1)$	n
P / DFT	$[0: n-1]$	$4 \times [0: n-1]$	$(0,4,8 \dots, 4n-4)$	n

Table 2 : Range selections in real (S_R) and Fourier space (S_{4F}) for various Discrete Transforms

4 – Evaluation of p (see equation (2)) with non-uniform BC

The fix-point algorithm described in equation (2) (left), summarizes in two steps: evaluate $p(\tilde{T})$, apply the Green operator ($\tilde{T} = G_D(p)$). The second step was the purpose of the previous section. The evaluation of p, described below, is done in real space using finite differences with the O- or H-scheme. Recall that p is defined on the grid of nodes, as well as $\tilde{T}$, with the range $[0: n]$.

4.1 – Evaluation with non-uniform Dirichlet or periodic BC and null Neumann BC

The definition of p is given in equation (2) and it is divided in two parts $p = p_1 - p_0$ with $p_1 = \mathrm{div_D}(\boldsymbol{q})$ and $p_0 = k_0 \left(\mathrm{div_D}\left(\boldsymbol{\nabla_D}\tilde{\boldsymbol{T}}\right)\right)$ where the norm of p_1 is used as convergence criterion. The important steps of the evaluation are reported below.

Step 1: Evaluating $\boldsymbol{\nabla_D \widetilde{T}}$

The derivation of $\tilde{T}$ using H-scheme, naturally gives the complete field of $\boldsymbol{\nabla_D \widetilde{T}}$ defined at centres (range $[0{:}\, n_d - 1]_{d=1:3}$). On the contrary, using the O-scheme, $\boldsymbol{\nabla_D \widetilde{T}}$ being defined at nodes (range $[0{:}\, n_d]_{d=1:3}$), it requires the knowledge of $\tilde{T}$ in the 6 planes (indices $i_d = -1$ and $i_d = n + 1$, for each direction d) surrounding the unit-cell. The value of $\tilde{T}$ for these additional points are evaluated according to the symmetry conditions, chosen in agreement with the choice of BC (see section 3.7).

Step 2: Evaluating $\mathrm{div}_{\mathrm{D}}\left(\boldsymbol{\nabla_D \widetilde{T}}\right)$

$\mathrm{div}_{\mathrm{D}}\left(\boldsymbol{\nabla_D \widetilde{T}}\right)$ is defined at nodes (range $[0{:}\, n_d]_{d=1:3}$). Using the O-scheme, $\boldsymbol{\nabla_D \widetilde{T}}$ being defined at nodes (with the same range $[0{:}\, n_d]_{d=1:3}$), it requires the knowledge of $\boldsymbol{\nabla_D \widetilde{T}}$ in the 6 surrounding planes (of nodes). Similarly, using the H-scheme requires the knowledge of $\boldsymbol{\nabla_D \widetilde{T}}$ in the 6 surrounding planes (of centres). In both cases, the symmetry conditions of $\boldsymbol{\nabla_D \widetilde{T}}$, deduced from the symmetry of $\tilde{T}$ in section 3.6, are used.

Step 3: Evaluating $\boldsymbol{q} = -\underline{K}.\left(\boldsymbol{\nabla_{\mathrm{D}} T^*} + \boldsymbol{\nabla_{\mathrm{D}} \widetilde{T}}\right)$.

The evaluation of $\boldsymbol{q}$ is very simple, and emphasis is put on the term $\boldsymbol{\nabla_{\mathrm{D}} T^*}$. Defined during the initialization, it allows for non-uniform Dirichlet or periodic BC.

For Dirichlet BC on both sides (i.e. WAWA symmetry), in a given direction d, 2D heterogeneous temperatures fields are imposed on the two opposite faces of the unit-cell, for example $T^*[0{,}0{:}\, n_2, 0{:}\, n_3]$ and $T^*[n_1, 0{:}\, n_2, 0{:}\, n_3]$ if $d = 1$. Any field compatible with these boundary conditions can be used for T^*, a simple linear interpolation is chosen. The same linear interpolation is used if Dirichlet BC are applied on 1, 2 or 3 couples of opposite faces.

For Dirichlet BC on one side and Neumann BC on the other side (i.e. WAWS or WSWA symmetry): the same linear interpolation is used, with the value of T^* on the Neumann side arbitrarily chosen equal to T^*on the Dirichlet side.

Finally, note that for the H-scheme, the definition of T^* on the range $[0{:}\, n_1, 0{:}\, n_2, 0{:}\, n_3]$ is sufficient to evaluate $\boldsymbol{\nabla_{\mathrm{D}} T^*}$ on the grid of centres. For the O-scheme, T^* must be defined on the range $[-1{:}\, n_1 + 1, -1{:}\, n_2 + 1, -1{:}\, n_3 + 1]$ to evaluate $\boldsymbol{\nabla_{\mathrm{D}} T^*}$ on the grid of nodes. The linear function used for the interpolation inside the unit-cell is kept for extrapolation at points located outside of the unit-cell.

For periodic BC, gradient fields $\boldsymbol{\nabla_{\mathrm{D}} T^*}$ as proposed for 2-sides Dirichlet BC, can be prescribed. As the temperature fluctuation $\tilde{T}$ is periodic, its 1D-average gradient in a given direction d is a null 2D field, so that the 1D-average gradient of the temperature T, in direction d, is equal to the 1D-average gradient of $\boldsymbol{T}^*$,in direction d.

Note that the specific case of uniform $\boldsymbol{\nabla_{\mathrm{D}} T^*}$, is extensively used in the context of first order homogenization, with both Dirichlet and periodic BC.

Step 4: Evaluation of $\mathrm{div}_{\mathrm{D}}(\boldsymbol{q})$

The same considerations as those described for step 2 (evaluation of $\mathrm{div}_{\mathrm{D}}\left(\boldsymbol{\nabla_D \widetilde{T}}\right)$) apply to step 4. However, it is worth noting that the symmetry conditions used for $\boldsymbol{\nabla_D \widetilde{T}}$ are also used for $\boldsymbol{q}$. Hence, a

WS symmetry condition on $\tilde{T}$, corresponding to a null-Neumann BC on $\boldsymbol{\nabla_D \widetilde{T}}$ (i.e. $\boldsymbol{\nabla_D \widetilde{T}}.\boldsymbol{n_d} = 0$), also corresponds to a null-Neumann BC on $\boldsymbol{q}$ (i.e. $\boldsymbol{q}.\boldsymbol{n_d} = 0$).

4.2 – Adding non-zero Neumann BC

As demonstrated above, using the DT framework and the set of equation (2) only allows to apply null-Neumann BC. The only way to introduce non-zero Neumann BC is to define an appropriate volume source field r^* null everywhere except at, or in the inner neighbourhood of, the boundary. In practice, r^* is defined by $r^* = \mathrm{div}_D(\boldsymbol{q}^*)$ with a flux $\boldsymbol{q}^*$, null everywhere in the unit-cell except at, or in the outer neighbourhood of, the boundary (precisions will be given below for the definition of $\boldsymbol{q}^*$, consistently with the applied fluxes). The definition of p is then modified according to:

$$\begin{cases} \boldsymbol{q} = -\underline{K}.\left(\boldsymbol{\nabla_D T}^* + \boldsymbol{\nabla_D \widetilde{T}}\right) + \boldsymbol{q}^* \\ p = \mathrm{div_D}\left(\boldsymbol{q} - k_0 \boldsymbol{\nabla_D \widetilde{T}}\right) \end{cases} \tag{14}$$

As a consequence, as soon as $\boldsymbol{q}^*$ is correctly initialized, the minor modification consists in adding $\boldsymbol{q}^*$ to $-\underline{K}.\left(\boldsymbol{\nabla_D T}^* + \boldsymbol{\nabla_D \widetilde{T}}\right)$ after step 3. Details about the initialization of $\boldsymbol{q}^*$ are given below, for a Neumann BC applied in direction 1, on the left side, so that the outer normal vector $\boldsymbol{N}$ is $-\boldsymbol{e_1}$ and $(\boldsymbol{q}.\boldsymbol{e_1})_{S_1^0} = (q_1)_{S_1^0} = -Q_1^*$ **,** with Q_1^* an applied outcoming heat flux (a 2D field in the most general case).

For the O-scheme, $\boldsymbol{q}$ being defined at nodes, the condition $(q_1)_{S_1^0} = -Q_1^*$ is prescribed at nodes and the range of the applied flux Q^*, is $[0\!:n_2, 0\!:n_3]$. As $\mathrm{div_D}$ is applied to $\boldsymbol{q}^*$, it must also be defined on planes of nodes surrounding the unit-cell, so the range of $\boldsymbol{q}^*$ is $[-1\!:n_{d+1}]_{d=1:3}$. $\boldsymbol{q}^*$ is null everywhere except, for the BC considered here, on the two first planes of nodes for which :

$$\begin{cases} q_1^*[-1,0\!:n_2, 0\!:n_3] = -2Q_1^*[0\!:n_2, 0\!:n_3] & \text{(first plane out of the unit} - \text{cell)} \\ q_1^*[0,0\!:n_2, 0\!:n_3] = -Q_1^*[0\!:n_2, 0\!:n_3] & \text{(boundary plane)} \end{cases} \tag{15}$$

Assuming, as in 4.1 - step 4, that $\widetilde{\boldsymbol{q}} = -\underline{K}.\left(\boldsymbol{\nabla_D T}^* + \boldsymbol{\nabla_D \widetilde{T}}\right)$ has the same symmetries as $\boldsymbol{\nabla_D \widetilde{T}}$, then a null-Neumann BC applies to $\widetilde{\boldsymbol{q}}$ in direction 1 so that $(\tilde{q}_1)_{S_1^0} = 0$. Hence, the choice $(q_1^*)_{S_1^0} = -Q_1^*$ made for the boundary plane (equation (15)) allows satisfying the expected Neumann BC $(q_1)_{S_1^0} = (\tilde{q}_1)_{S_1^0} + (q_1^*)_{S_1^0} = -Q_1^*$. The choice $q_1^* = -2Q_1^*$ made for the first plane out of the unit-cell, is done to respect the condition that the derivative evaluated at the boundary with the O-scheme, $\left(\frac{dq_1^*}{dx_1}\right)_{S_1^0} = \frac{q_1^*[1,0:n_2,0:n_3] - q_1^*[-1,0:n_2,0:n_3]}{2dx_1} = \frac{-q_1^*[-1,0:n_2,0:n_3]}{2dx}$, should be equal to the derivative evaluated from nodes located inside the cell, $\left(\frac{dq_1^*}{dx_1}\right)_{S_1^0} = \frac{q_1^*[1,0:n_2,0:n_3] - q_1^*[0,0:n_2,0:n_3]}{dx_1} = \frac{-q_1^*[0,0:n_2,0:n_3]}{dx_1} = \frac{Q_1^*}{dx_1}$.

For the H-scheme, $\boldsymbol{q}$ being defined at centres, the condition $(q_1)_{S_1^0} = -Q_1^*$ is prescribed at the middle points of two centres separated by the unit-cell boundary. Hence, the range of the applied flux Q^* is $[0\!:n_2 - 1, 0\!:n_3 - 1]$. As $\mathrm{div_D}$ is applied to $\boldsymbol{q}^*$, it must also be defined on planes of centres surrounding the unit-cell, so the range of $\boldsymbol{q}^*$ is $[-1\!:n_d]_{d=1:3}$. $\boldsymbol{q}^*$ is null everywhere except, for the BC considered here, on the first plane of centres (outside the unit-cell) for which :

$$q_1^*[-1,0\!:n_2 - 1, 0\!:n_3 - 1] = -2Q_1^*[0\!:n_2 - 1, 0\!:n_3 - 1] \tag{16}$$

With this choice, the flux at the boundary, located in the middle of the two centres consists of $(q_1)_{S_1^0} = (\tilde{q}_1)_{S_1^0} + (q_1^*)_{S_1^0}$, with $(q_1^*)_{S_1^0} = \frac{q_1^*[-1,0:n_2-1,0:n_3-1]+q_1^*[0,0:n_2-1,0:n_3-1]}{2} = \frac{0-2Q_1^*}{2} = -Q_1^*$ and $(\tilde{q}_1)_{S_1^0} = 0$ (as a null-Neumann BC is imposed to $\widetilde{\boldsymbol{q}}$, see section 4.1 – step 4). Hence, the expected Neumann BC, $(q_1)_{S_1^0} = -Q_1^*$, is satisfied.

Here, attention must be paid to the points located at the edges of the domain $[-1,-1:n_2,-1:n_3]$, which are not considered in equation (16). They must be filled with the symmetry conditions associated to $\boldsymbol{\nabla_D}\widetilde{\boldsymbol{T}}$ in direction 2 and 3. This remark holds for the H-scheme. For the O-scheme, the points at the edges are not used to evaluate $\mathrm{div_O}(\boldsymbol{q}^*)$ so that applying these symmetry conditions is not mandatory.

The definition of $\boldsymbol{q}^*$ proposed here for a non-zero Neumann BC on face S_1^0 can be easily extended to any other face. Submitted to a non-zero Neumann BC

5 – Additional remarks

5.1 – A proof of concept

The implementation made of the FFT-based method used for the validation tests, is a proof of concept demonstrating its flexibility. The user defined inputs are:

- the discrete thermal conductivity field defined on the whole unit-cell,
- for each couple of opposite faces, the choice of BC (Dirichlet/Dirichlet, Dirichlet/Neumann, Neumann/Dirichlet, Neumann/Neumann or Periodic BC corresponding to the 5 possible symmetry conditions WAWA, WAWS, WSWA, WSWS and P),
- the fields T^* and $\boldsymbol{q}^*$ associated respectively to the Dirichlet and Neumann BC,
- the FD scheme chosen between the O- and the H-scheme.

The proposed implementation is then able to simulate any of the configurations given by these inputs. Considering the choice of BC, it must be emphasized that $5 \times 5 \times 5 = 125$ different types of BC can be prescribed.

This proof of concept relies on the *matlab* language, and the toolbox *matlab-dtts* proposed by Treeby [18], who implemented an interface with the 8 Discrete Sine and Cosine Transforms available in the library *fftw* [5].

The next step will consist of implementing this method in the massively parallel AMITEX code [8].

5.2 – Convergence criterion

The convergence criterion, associated to the equilibrium equation $\mathrm{div_D}(\boldsymbol{q}) = 0$, reads:

$$\varepsilon = \frac{\|\mathrm{div_D}(\boldsymbol{q})\|_{L^2}}{\left\|\frac{\boldsymbol{q}}{dx}\right\|_{L^2}} < \varepsilon^0 \tag{17}$$

with dx the voxel size. The iterative algorithm is interrupted as soon as this criterion is satisfied.

5.3 – Convergence Acceleration

The convergence acceleration technique proposed by Anderson [3], implemented in the code AMITEX [8] to accelerate the FFT-based fix-point algorithm [4], is also implemented here with a depth of 3 and an acceleration every 3 iterations. Briefly, it consists of saving in a buffer the last 4 couples of solution and residual fields, and to propose every 3 iterations, a new solution field deduced from the saved fields (see [4], for a more detailed description).

5.4 – Discussion

In the present paper, choice is made to evaluate $p = \mathrm{div}_{\mathrm{D}}\left(\boldsymbol{q} - k_0 \boldsymbol{\nabla_{\mathrm{D}}} \widetilde{\boldsymbol{T}}\right)$ in real space and then perform a DT, apply the Green operator in Fourier space and inverse DT to obtain $\tilde{T}$. Another, and more usual way, is to evaluate $\boldsymbol{q}$, perform the DTs, apply the Green operator (different from the one presented here) and inverse DTs to obtain $\boldsymbol{\nabla_{\mathrm{D}}} \widetilde{\boldsymbol{T}}$.

In the first implementation, DT/inverse DT are performed on a scalar field, for the second, they are performed on vector fields and the number of DT/inverse DT is multiplied by 3.

The arguments for reducing the number of DT/iDT are the following:

- The H- and O-schemes proposed here are very 'local' (8 or 6 points are involved in the derivation operators) and it can be more efficient to apply derivatives in real space, instead of applying additional transforms and inverse transforms.
- This point is reinforced when using Discrete Sine and Cosine Transforms, whose implementation in the library *fftw* is, according to the authors, less efficient than DFT.
- It is also reinforced when dealing with a massively parallel implementation (the next target after this proof of concept). Actually, with data distributed over a 2D pencil decomposition as in [8], the 3D transform requires a transposition of data to perform the 1D transforms in each direction. This transposition corresponds to a "ALLTOALL" communication between all the processes that comes with an additional communication cost.

6 – Validation

As simulations performed with the H-scheme are equivalent to Finite Element simulations with linear hexaedral finite elements (Hex8R) [14], a quantitative cross validation can be made by comparisons of strictly equivalent simulations performed with the FE and FFT-based codes. For that purpose a cubic unit-cell (dimension $1 \times 1 \times 1$) is used, with a non-centred spherical inclusion (radius 0.3, centre at $(0.15,0.4,0.6)$, see Figure 2). The unit-cell is simple but non-symmetric, with the inclusion crossing the boundary. This choice allows to demonstrate that the method is not limited to unit-cells with inner symmetries and that it is capable to account for material discontinuities located at the boundary. To enforce strong heterogeneities a high contrast is chosen for the thermal conductivity (matrix 1, inclusion 10^{-3}). The unit-cell is discretized with 32x32x32 voxels. A high accuracy is prescribed for this validation (convergence criterion $\varepsilon^0 = 10^{-8}$).

Note that all the simulations below have been performed with a single flexible implementation that allows to choose between 125 types of symmetries and 2 finite difference schemes. A selection of loadings of increasing complexity is proposed below. Table 3 gathers the different loadings used in the following sub-sections.

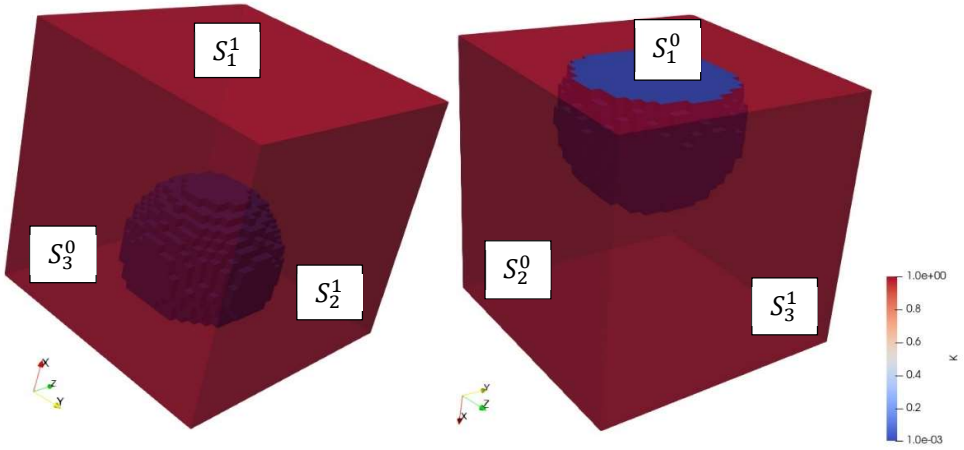

Figure 2 : Thermal conductivity field corresponding to a resistive spherical inclusion of radius 0.3, centred at (0.15, 0.4, 0.6) in a 1x1x1 unit-cell. The six different faces S_d^i, used to apply various loadings with either periodic, Dirichlet or Neumann BC are reported.

Test name	S_1^0	S_1^1	S_2^0	S_2^1	S_3^0	S_3^1
Periodic	$T(0,x_2,x_3) = x_2 + x_3 + \tilde{T}(0,x_2,x_3)$	$T(L_1,x_2,x_3) = L_1 + x_2 + x_3 + \tilde{T}(L_1,x_2,x_3)$	$T(x_1,0,x_3) = x_1 + x_3 + \tilde{T}(x_1,0,x_3)$	$T(x_1,L_2,x_3) = x_1 + L_2 + x_3 + \tilde{T}(x_1,L_2,x_3)$	$T(x_1,x_2,0) = x_1 + x_2 + \tilde{T}(x_1,x_2,0)$	$T(x_1,x_2,L_3) = x_1 + x_2 + L_3 + \tilde{T}(x_1,x_2,L_3)$
Dirichlet	$T(0,x_2,x_3) = x_2 + x_3$	$T(L_1,x_2,x_3) = L_1 + x_2 + x_3$	$T(x_1,0,x_3) = x_1 + x_3$	$T(x_1,L_2,x_3) = x_1 + L_2 + x_3$	$T(x_1,x_2,0) = x_1 + x_2$	$T(x_1,x_2,L_3) = x_1 + x + L_3$
Neumann	$q_1(0,x_2,x_3) = 1$	$q_1(L_1,x_2,x_3) = 1$	$q_2(x_1,0,x_3) = 1$	$q_2(x_1,L_2,x_3) = 1$	$q_3(x_1,x_2,0) = 1$	$q_3(x_1,x_2,L_3) = 1$
Per./Dir./Neu.	$T(0,x_2,x_3) = x_2 + x_3 + \tilde{T}(0,x_2,x_3)$	$T(L_1,x_2,x_3) = L_1 + x_2 + x_3 + \tilde{T}(L_1,x_2,x_3)$	$T(x_1,0,x_3) = x_1 + x_3$	$T(x_1,L_2,x_3) = x_1 + L_2 + x_3$	$q_3(x_1,x_2,0) = 1$	$q_3(x_1,x_2,L_3) = 1$
Neu-Dir/Dir/Neu	$q_1(0,x_2,x_3) = 1$	$T(L_1,x_2,x_3) = L_1 + x_2 + x_3$	$T(x_1,0,x_3) = x_1 + x_3$	$T(x_1,L_2,x_3) = x_1 + L_2 + x_3$	$q_3(x_1,x_2,0) = 1$	$q_3(x_1,x_2,L_3) = 1$
Dir-Neu/Dir/Neu	$T(0,x_2,x_3) = x_2 + x_3$	$q_1(L_1,x_2,x_3) = 1$	$T(x_1,0,x_3) = x_1 + x_3$	$T(x_1,L_2,x_3) = x_1 + L_2 + x_3$	$q_3(x_1,x_2,0) = 1$	$q_3(x_1,x_2,L_3) = 1$
Non-uniform	$T(0,x_2,x_3) = T^*(0,x_2,x_3)$	$q_1(L_1,x_2,x_3) = Q_1^*(L_1,x_2,x_3)$	$q_2(x_1,0,x_3) = 0$	$q_2(x_1,L_2,x_3) = 0$	$q_3(x_1,x_2,0) = 0$	$q_3(x_1,x_2,L_3) = 0$

Table 3 : Description of the loading cases used for the validation of the method. The unit-cell and the faces S_d^i are defined in Figure 2. For the "periodic" case, $\tilde{T}$ is periodic (equal on opposite faces). For the "non-uniform" case, T^* and Q_1^* are defined in section 6.3. For the other cases, applied $\boldsymbol{G}^*$ or $\boldsymbol{Q}^*$ (see definition in section 6.1) are set to one, leading to the BC reported in the present table.

6.1 – Uniform loadings with full Periodic, Dirichlet and Neumann BC.

The loadings considered here are given by, for all x at the boundary of the unit-cell, $T(\boldsymbol{x}) = \boldsymbol{G}^*.\boldsymbol{x} + \tilde{T}(\boldsymbol{x})$, $\tilde{T}$ submitted to null-Dirichlet or periodic BC, or $\boldsymbol{q}(\boldsymbol{x}).\boldsymbol{N}(\boldsymbol{x}) = \boldsymbol{Q}^*.\boldsymbol{N}(\boldsymbol{x})$ for Neumann BC. They are called 'uniform' in the sense that $\boldsymbol{G}^*$ and $\boldsymbol{Q}^*$ are uniforms over the unit-cell. Such loadings are commonly used in the homogenization context as they provide respectively, an upper bound, an

estimate and a lower bound, for the homogenized conductivity. It is easily demonstrated that $\overline{\boldsymbol{\nabla T}} = \boldsymbol{G}^*$ for periodic and Dirichlet BC and $\bar{\boldsymbol{q}} = \boldsymbol{Q}^*$for Neumann BC. In the simulations below the loadings are applied with $G_1^* = G_2^* = G_3^* = Q_1^* = Q_2^* = Q_3^* = 1$.

Finite element simulations are performed with the FE code CAST3M [1], using Hex8R elements. Table 4 gathers the average heat flux and temperature gradient for the three FE simulations and the relative error (definition in the table legend) between FE and FFT-based simulation. As expected, the relative error is very low with a maximum value of less than 10^{-8} for Neumann simulation. This is consistent with the low value of the criterion of 10^{-8} used in the FFT-based algorithm. The precision on the average temperature gradient is null for Dirichlet and periodic BC: actually this quantity is strictly imposed by the algorithm. On the contrary, for Neumann BC, the applied flux is not strictly applied by the algorithm and the precision of the average flux depends on the convergence criterion. At last, the maximum relative error is by far the error on $\overline{\nabla T}_1$ for the Neumann BC. It is related to the fact that, on face S_1^0, a constant heat flux is applied directly to the inclusion whose conductivity is very low. That induces very large (and heterogeneous) temperature gradient as observed in the table (when comparing $\overline{\nabla T}_1$ to the other components). The higher number of iterations also reveals that the Neumann BC simulation (with the low conductive inclusion crossing the boundary) is more delicate.

	It.	Factor	$\overline{\nabla T}_1$	$\overline{\nabla T}_2$	$\overline{\nabla T}_3$	$\bar{q}_1$	$\bar{q}_2$	$\bar{q}_3$
Periodic	47		1.000	1.000	1.000	-0.8430	-0.8669	-0.8661
Rel. error		10^{-11}	*0.00*	*0.00*	*0.00*	*0.12*	*0.02*	*0.86*
Dirichlet	46		1.000	1.000	1.000	-0.8772	-0.8732	-0.8760
Rel. error		10^{-10}	*0.00*	*0.00*	*0.00*	*0.50*	*0.29*	*0.24*
Neumann	152		-20.72	-1.192	-1.183	1.000	1.000	1.000
Rel. error		10^{-8}	*0.76*	*0.01*	*0.01*	*0.00*	*0.02*	*0.02*
Per/Dir/Neu	49		1.000	1.000	-0.0037	-0.8444	-0.8779	0.0022
Rel. error		10^{-7}	*0.*	*0.*	*0.28*	*0.00*	*0.00*	*0.50*
Neu-Dir/Dir/Neu	117		-19.17	1.000	0.1773	-0.4170	-0.8206	-0.1706
Rel. error		10^{-7}	*0.15*	*0.00*	*0.00*	*0.01*	*0.00*	*0.00*
Dir-Neu/Dir/Neu	48		0.4700	1.000	0.1833	-0.3969	-0.8828	-0.1209
Rel. error		10^{-10}	*0.13*	*0.00*	*0.93*	*0.05*	*0.01*	*0.80*
Non-uniform	75		-0.3240	0.0170	-0.0170	0.2500	-0.0071	0.0071
Rel. error		10^{-9}	*0.05*	*0.10*	*0.10*	*0.02*	*0.42*	*0.42*

Table 4 : Average temperature gradient and heat flux evaluated with a FE code (CAST3M) for the various loadings, and the relative error comparing FE and FFT-based simulation (with a convergence criterion $\varepsilon^0 = 10^{-8}$). The relative error is defined, for each component i, by $\frac{|\bar{X}_i^{EF} - \bar{X}_i^{FFT}|}{|\bar{X}_i^{EF}|}$, $\bar{X}$ being the average temperature gradient $\overline{\nabla T}_i$ or the average flux $\bar{q}_i$.

6.2 – Uniform loadings with combined Periodic, Dirichlet and Neumann BC.

Combined BC are now considered with Periodic/Dirichlet/Neumann BC in directions 1/2/3. The uniform applied load is given by $G_1^* = G_2^* = G_3^* = 1$ and $Q_3^* = 1$. Results in Table 4 validate the FFT-based simulation with a relative error below 10^{-7} (this value is larger than the others but $\overline{\nabla T}_3$ and $\bar{q}_3$ are also much smaller in this case). It can be noticed that, as mentioned before, $\overline{\nabla T}_1$and $\overline{\nabla T}_2$ are strictly imposed by periodic and Dirichlet BC in directions 1 and 2 ($\overline{\nabla T}_1 = G_1^*, \overline{\nabla T}_2 = G_2^*$), whereas $\bar{q}_3$ is very

different from Q_3^*, the heat flux imposed by Neumann BC in direction 3. To explain it, the expression of the average heat flux, using the equilibrium equation, is given below:

$$V\bar{\boldsymbol{q}} = \int_\Omega \boldsymbol{q}\,\mathrm{dV} = \int_\Omega \boldsymbol{x}\,(\boldsymbol{q}.\boldsymbol{N})\mathrm{dS} \\ = \int_{S_1} L_1 q_1^1 \boldsymbol{e_1} + (x_2\boldsymbol{e_2} + x_3\boldsymbol{e_3})(q_1^1 - q_1^0)\,\mathrm{dS} + \int_{S_2} \ldots + \int_{S_3} \ldots \tag{18}$$

where q_1^0 and q_1^1 are the heat fluxes (1st component) on the two opposites faces S_1^0 and S_1^1. Integration in these 2 opposites faces in direction 1, is symbolically gathered in S_1. For Neumann and periodic BC $q_1^1 - q_1^0 = 0$: the contribution of the BC (on faces S_1) to the average heat flux is only in direction 1, and equal to $Q_1^*\boldsymbol{e_1}$ for Neumann BC. For Dirichlet BC, fluxes on opposite faces can be different, giving rise to a possible coupling with the other directions. As the inclusion is not centered on the face S_1^0, this explains the difference observed between $\bar{\mathrm{q}}_3$ and Q_3^*.

Up to now, simulations were performed with the same condition on both sides, we now consider the cases of Neumann and Dirichlet BC on opposite faces, here in direction 1. Direction 2 and 3 are still submitted to Dirichlet and Neumann BC. The uniform applied load is given by $G_1^* = G_2^* = G_3^* = 1$ and $Q_1^* = Q_3^* = 1$. Results in Table 4 about these two new tests case, with a maximum relative error of 10^{-7}, validates the implementation with Neumann and Dirichlet BC on opposite faces. Note that, consistently with previous observation, the error and the number of iterations are larger when the Neumann BC is applied to the face crossed by the low conducting inclusion.

6.3 – Non-uniform (and combined) loadings

The case of non-uniform loadings is now considered in direction 1, combined with null flux Neumann BC on the four other faces (directions 2 and 3). Dirichlet BC is applied on surface S_1^0 with the temperature prescribed by $T(\boldsymbol{x}) = T^*(\boldsymbol{x}) = T_0\left(1 - \left(\frac{x_2 - 1/2}{1/2}\right)^2\left(\frac{x_3 - 1/2}{1/2}\right)^2\right)$. On the opposite face S_1^1, the flux is null except on a square of size 0.5×0.5, centred on the face. The comparison with FE simulations, on the average gradient and heat flux in Table 4, reveals errors lower than 10^{-9}. As expected from equation (16) and the chosen BC, the average flux in direction 1, $\bar{q}_1$, is equal to $Q^*/4$ (Q^* being applied on a surface of size 0.5×0.5). The non-vanishing values for $\bar{q}_2$ and $\bar{q}_3$ is explained once again by the coupling arising when using Dirichlet BC (see equation(16)).

For this non-uniform case, a relative error on the complete flux fields is also evaluated with $E = \|q^{FE} - q^{FFT}\|_{L^2} / \|q^{FE}\|_{L^2}$. The values, gathered in Table 5 for different convergence criteria, confirms, now on full fields, that the error is very low and reduces with the convergence criteria.

ε^0	10^{-6}	10^{-8}	10^{-10}
E	$1.2\ 10^{-4}$	$8.6\ 10^{-7}$	$8.6\ 10^{-9}$

Table 5 : Relative error E on flux fields between FE and FFT-based simulations for difference convergence criteria ε^0.

The flux fields q_1, given in Figure 3, allows visualizing the applied heat flux on a square region on face S_1^1 (right image) and, indirectly, the non-uniform Dirichlet BC with the applied parabolic profile on face

S_1^0 (left image). The inclusion having a very low thermal conductivity, the heat flux is almost equal to zero.

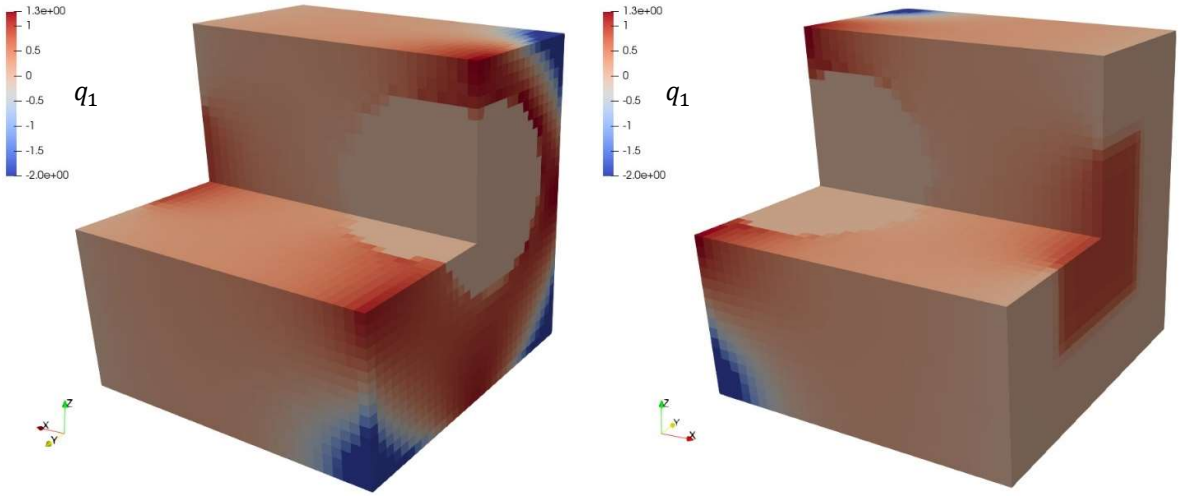

Figure 3 : Heat flux field q_1 for the non-uniform loading

6.4 – Simulations with the O-scheme

For the O-scheme, without any appropriate FD code that could provide a rigorous comparison with FFT-based results, validation is then reduced to a comparison between FFT-based simulations performed with the O- and H-schemes. Average heat flux and temperature gradient are compared quantitatively as a function of the spatial resolution in Table 6. As expected, the difference decreases when increasing the spatial resolution, both simulations converge towards the solution. The largest difference is observed with Neumann BC, especially when applied to the face crossing the low conducting inclusion. For all the simulations, it has been observed that the H-scheme converge faster than the O-scheme, and the evolution of the differences in Table 6 is mostly due to the O-scheme. As an example, for the full-Neumann BC simulation, $\overline{\nabla T}_1$ evolves between -20.72 and -20.61 when increasing the resolution from 32 to 128, for the H-scheme, and between -16.30 and -19.56 for the O-scheme.

To complete qualitatively this validation, the heat flux field q_1 evaluated for the non-uniform loading with the O-scheme, is displayed in Figure 4. It compares very well with Figure 3, obtained with the H-scheme.

	32	64	128
Periodic	0/0.0093	0/0.0045	0/0.0024
Dirichlet	0/0.001	0/5.34 10^{-4}	0/4.82 10^{-4}
Neumann	4.4151/0.	2.0259/0	1.0503/0
Per/Dir/Neu	0.0612/0.0066	0.0308/0.0033	0.0155/0.0017

Table 6 : Difference between O- and H-schemes on the average temperature gradient and flux ($\|\delta\overline{\boldsymbol{\nabla T}}\| / \|\delta\overline{\boldsymbol{q}}\|$)

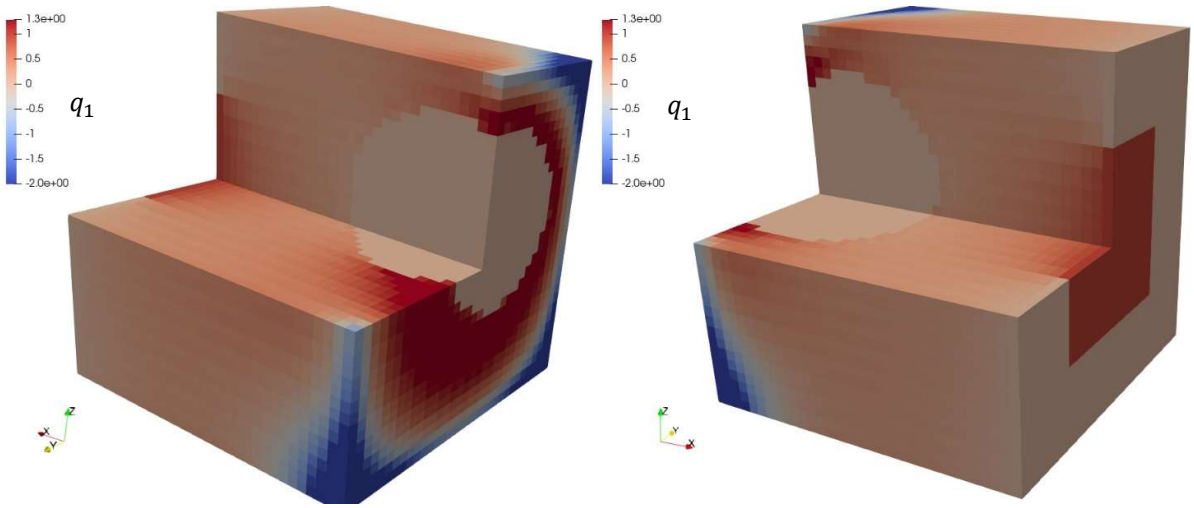

Figure 4 : Heat flux field q_1 for the non-uniform loading, obtained with the 0-scheme

7 – Conclusions

A flexible FFT-based implementation has been proposed to extend its usage from periodic BC to any type of the 5 BC applied to each couple of faces: Dirichlet/Dirichlet, Dirichlet/Neumann, Neumann/Dirichlet, Neumann/Neumann and Periodic. All these conditions can be associated with any non-uniform loading. The implementation relies on two important points.

The first point concerns the use of discrete sine and cosine transforms, whose definition can be linked to the definition of discrete Fourier transform applied to a 4 times extended signal, using appropriate symmetries. Hence, the periodic Green operator can be applied to this extended signal for an appropriate selection of wave vectors. Besides, the discrete sine or cosine transforms have also to be performed on an appropriate selection of grid points. With these two selection operators, the discrete Green operator, associated to any set of symmetry conditions, can be easily applied.

The second point is the term p (see equation (2)), evaluated in real space using discrete derivation schemes and taking into account the appropriate symmetries, it also introduces the non-uniform loading through the quantities T^* and $\boldsymbol{q}^*$ whose definition is associated to Dirichlet (and periodic) and Neumann BC, respectively.

This flexible implementation has been validated from a cross-comparison between FFT-based simulations, using the H-scheme for discrete derivation, and a FE simulations, using linear hexahedral elements with reduced integration. As expected from these strictly equivalent simulations [14], the simulations provide the same results, up to the precision of the FFT-based iterative algorithm. The validation has been performed on various types of loadings: uniform loadings with full or combined Dirichlet, periodic or Neumann BC, with non-uniform loadings and Dirichlet/Neumann or Neumann/Dirichlet BC on opposite faces.

The implementation also proposes two different types of Finite Difference schemes: the H-scheme, for which the derivation operator changes the support from a grid of nodes to a grid of centres, or vice-versa, and the O-scheme, for which all quantities are defined on the same grid (of nodes). It should pave the way to implement other FD schemes.

From the simulations performed with a low conductivity inclusion (contrast 1000 with the matrix) crossed by the boundary, and a very high precision ($\varepsilon^0 = 10^{-8}$), various remarks can be made: the number of iterations is very reasonable (between 46 and 152) and it is higher when Neumann BC are applied to the face crossed by the inclusion (in agreement with intuition). The present implementation appears much more efficient than using a buffer zone to apply Dirichlet BC [6]. Limited to unit-cells with parallelepiped shapes, the present method is not able to deal with volumes with arbitrary shapes and in that case using a buffer zone [6] [17] [16] remains an interesting solution. It also extends the capabilities of the method proposed recently [11] to non-uniform loadings as well as Dirichlet/Neumann BC on opposite faces.

As future prospects, the present implementation proposed in the context of conducting materials is a first step towards mechanical problems. Besides, the present proof of concept implemented through the *matlab* language, will have to be introduced in the FFT-based simulation code AMITEX [8] to take benefit of its massively parallel implementation.

Acknowledgments

The author would like to thank Marc Josien from CEA-Cadarache for fruitful discussions and Olivier Fandeur from CEA-Saclay who introduced reduced integration elements for thermal problems in the FE code CAST3M, required for the cross validation between FE and FFT codes.

APPENDIX: Symmetries of discrete signals and corresponding Discrete Trigonometric Transforms : graphical representations.

The figures below give different examples of symmetries for discrete signals, symmetries that are implicitly assumed when using the corresponding Discrete Trigonometric Transforms.

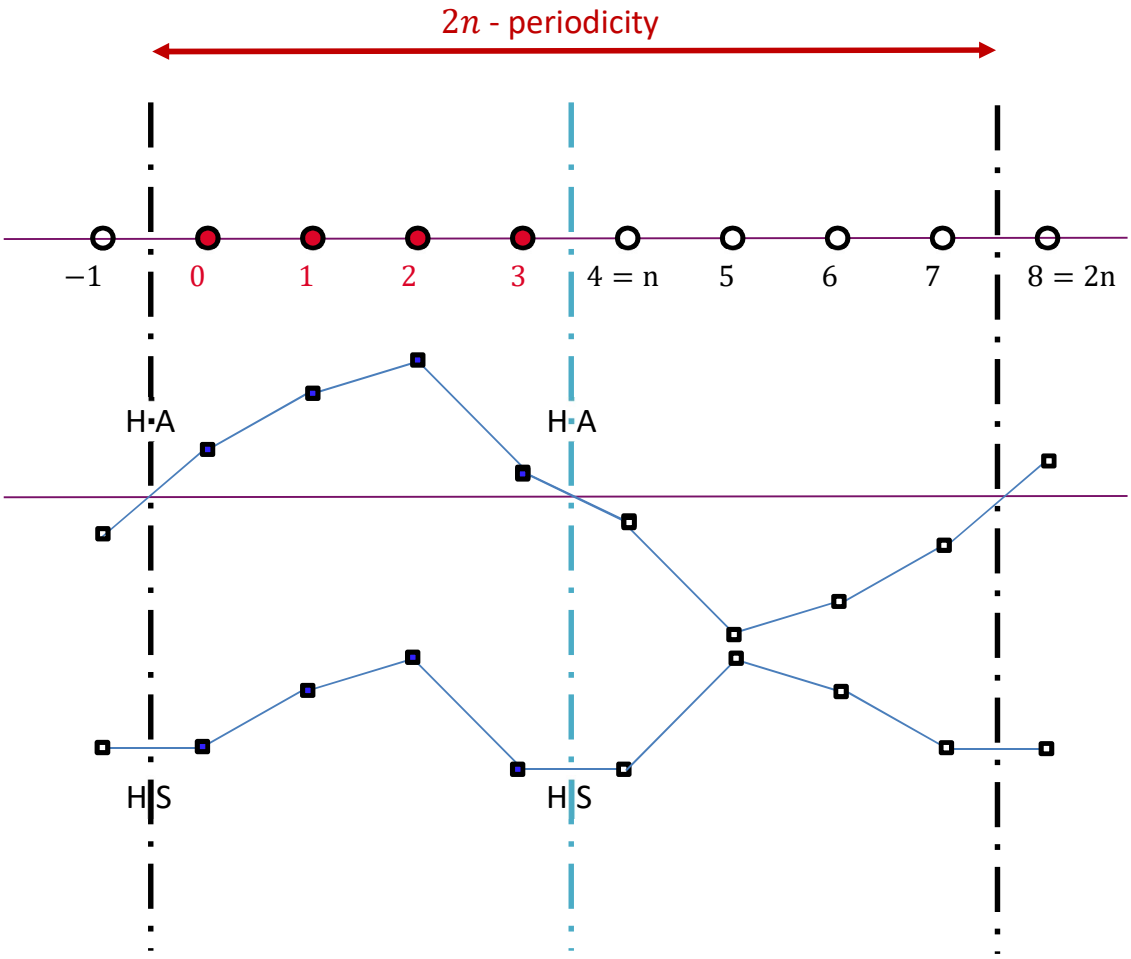

Figure 5 : Discrete signal with symmetry HAHA (upper) or HSHS (lower). The symmetrized signal has a 2n period. HAHA corresponds to DST2 and HSHS to DCT2 (according to the fftw definition used in the present paper).

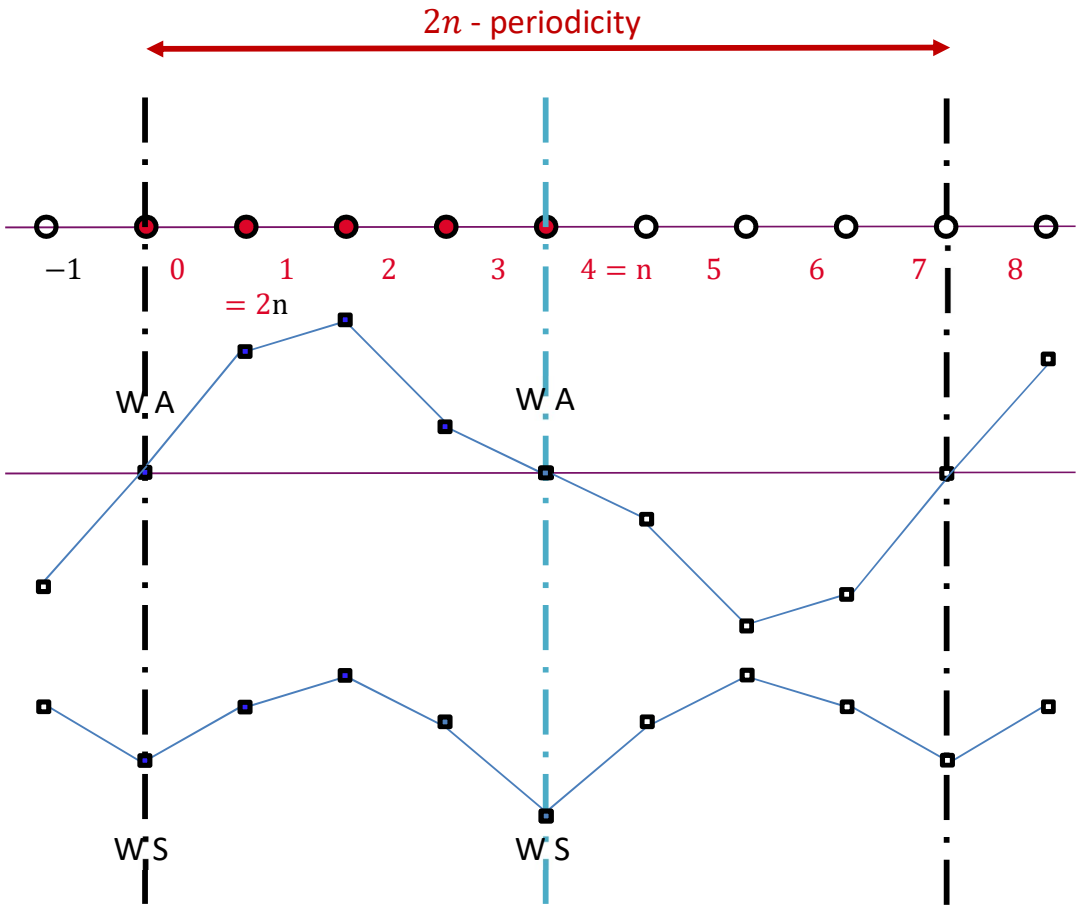

Figure 6 : Discrete signal with symmetry WAWA (upper) or WSWS (lower). The symmetrized signal has a 2n period. WAWA corresponds to DST1 and WSWS to DCT1 (according to the fftw definition used in the present paper).

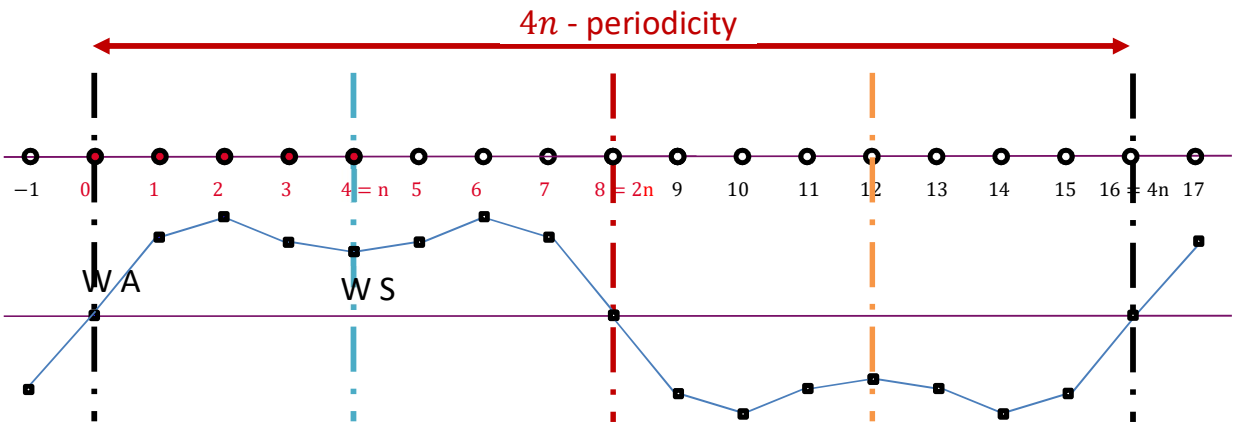

Figure 7 : Discrete signal with symmetry WAWS. The symmetrized signal has a 4n period. WAWS corresponds to DCT3 (according to the fftw definition used in the present paper).

Bibliography

[1] Cast3m, ww-cast3m.cea.fr.

[2] Wiegmann A. Fast poisson, fast helmholtz and fast linear elastostatic solvers on rectangular parallelepipeds. Technical report, Lawrence Berkeley National Lab. (LBNL), Berkeley, CA (United States), 1999.

[3] D.G. Anderson. Iterative procedures for nonlinear integral equations. *Journal of the ACM (JACM)*, 12(4):547–560, 1965.

[4] Y. Chen, L. Gélébart, C. Chateau, M. Bornert, C. Sauder, and A. King. Analysis of the damage initiation in a sic/sic composite tube from a direct comparison between large-scale numerical simulation and synchrotron x-ray micro-computed tomography. *Int. J. Solids Struct.*, 161:111 – 126, 2019.

[5] M. Frigo and S. G. Johnson. The design and implementation of fftw3. *Proceedings of the IEEE*, 93(2):216–231, 2005.

[6] Lionel Gélébart. A modified fft-based solver for the mechanical simulation of heterogeneous materials with dirichlet boundary conditions. *Comptes Rendus. Mécanique*, 348(8-9):693–704, 2020.

[7] Christian Gierden, Julian Kochmann, Johanna Waimann, Bob Svendsen, and Stefanie Reese. A review of fe-fft-based two-scale methods for computational modeling of microstructure evolution and macroscopic material behavior. *Archives of Computational Methods in Engineering*, 29(6):4115–4135, 2022.

[8] Lionel Gélébart. https://amitexfftp.github.io/amitex/index.html. 2022.

[9] Hannes Grimm-Strele and Matthias Kabel. Fft-based homogenization with mixed uniform boundary conditions. *Int J Numer Methods Eng*, 122(23):7241–7265, December 2021.

[10] Sergio Lucarini, Manas Vijay Upadhyay, and Javier Segurado. Fft based approaches in micromechanics: fundamentals, methods and applications. *Modelling and Simulation in Materials Science and Engineering*, 2021.

[11] V. Monchiet and G. Bonnet. Fft based iterative schemes for composite conductors with uniform boundary conditions. *European Journal of Mechanics - A/Solids*, 103:105146, 2024.

[12] H. Moulinec and P. Suquet. A numerical method for computing the overall response of nonlinear composites with complex microstructure. *Computer Methods In Applied Mechanics and Engineering*, 157(1-2):69–94, April 1998.

[13] D. Pahr and P. Zysset. Influence of boundary conditions on computed apparent elastic properties of cancellous bone. *Biomechanics and Modeling in Mechanobiology*, 7(6):463–476, 2008.

[14] M. Schneider, D. Merkert, and M. Kabel. Fft-based homogenization for microstructures discretized by linear hexahedral elements. *International Journal for Numerical Methods in Engineering*, 109(10):1461–1489, 2017.

[15] Matti Schneider. A review of nonlinear fft-based computational homogenization methods. *Acta Mechanica*, 232(6):2051–2100, 2021.

[16] Quy Dong To and Guy Bonnet. Fourier transform approach to homogenization of frequency-dependent heat transfer in porous media. *International Journal of Numerical Methods for Heat & Fluid Flow*, 33(6):2023–2048, January 2023.

[17] Quy-Dong To, Guy Bonnet, and Trung Nguyen-Thoi. Fourier transform approach to nonperiodic boundary value problems in porous conductive media. *Int J Numer Methods Eng*, 122(18):4864–4885, September 2021.

[18] B. E. Treeby. Matlab discrete trigonometric transform library. *https://github.com/ucl-bug/matlab-dtts, Last accessed on 2023-10-3*, 2020.

[19] F. Willot. Fourier-based schemes for computing the mechanical response of composites with accurate local fields. *Comptes Rendus Mécanique*, 343(3):232 – 245, 2015.

[20] Elliott S. Wise, Jiri Jaros, Ben T. Cox, and Bradley E. Treeby. Pseudospectral time-domain (pstd) methods for the wave equation: Realizing boundary conditions with discrete sine and cosine transforms. *J. Theor. Comp. Acout.*, 29(04):2050021, October 2020.